

TECHNICAL NOTE

D-1890

MEASUREMENT OF THE HEAT TRANSFER TO BODIES OF REVOLUTION
IN FREE FLIGHT BY USE OF A CATCHER CALORIMETER

By Gary T. Chapman and Charles T. Jackson, Jr.

Ames Research Center
Moffett Field, Calif.

LIBRARY
National Aeronautics and Space Administration

NATIONAL AERONAUTICS AND SPACE ADMINISTRATION
WASHINGTON

July 1963

NATIONAL AERONAUTICS AND SPACE ADMINISTRATION

TECHNICAL NOTE D-1890

MEASUREMENT OF THE HEAT TRANSFER TO BODIES OF REVOLUTION

IN FREE FLIGHT BY USE OF A CATCHER CALORIMETER

By Gary T. Chapman and Charles T. Jackson, Jr.

SUMMARY

A new experimental technique has been used to study the total heat transfer to a hemisphere and a blunted cone.

Aluminum models were gun-launched at speeds up to 11,000 fps, allowed to decelerate aerodynamically to a few hundred feet per second, and caught, and the total aerodynamic heat input was measured in the recovered models with a calorimeter.

These measurements showed that for the trajectories flown, that portion of the initial kinetic energy which goes into heating the body was larger for the configuration with the smaller drag. The data were further analyzed on the basis of the trajectories traversed, yielding heat-transfer rates as a function of velocity. These rates for the various configurations were compared with one another and again showed that the configuration with the higher drag had the lower heating rates. Further, the experimental heating rates for the hemisphere agreed well with the theoretical convective heating of the front face.

INTRODUCTION

Although ballistic ranges have been used to measure a wide variety of aerodynamic properties of free-flight models, they have seen comparatively little use for measurement of convective heating. The rather obvious reason for this is that it is difficult to determine accurately, by external observations, the rate of temperature rise of the model surface, either grossly or in detail. Although considerable effort has been made to develop miniature telemeter systems for this use, the comparatively little data which has been obtained indicates the difficulty of this approach, particularly at the high speeds where the heat transfer is of most interest. One system which has been used successfully is described in reference 1. It makes use of a thermocouple in the model nose to generate an electric current in a coil inside the model, the strength of the current being

proportional to the temperature rise of the thermocouple. The current generates an external magnetic field which is measured by detecting coils at several stations of the range to indicate the rate of heating.

This paper presents a different approach to the measurement of convective heating in a ballistic range, which was originally suggested to the authors by Mr. Alvin Seiff. The method is based on the recovery at low speeds of a test model at the end of a flight, after it has been decelerated from a high initial velocity by aerodynamic drag. The heat content of the recovered model is accurately measured in a calorimeter, and from a series of such shots at various launch velocities, the measurements can be analyzed to yield values of heat-transfer rates, averaged over the wetted area, as a function of velocity.

The purpose of this report is twofold: First, to present this new experimental method and to check the results of the method for the case of a hemisphere against proven theoretical results; second, to make comparison of the convective heat-transfer characteristics of a hemisphere, and a round-nosed cone of 60° included angle.

SYMBOLS

A_c	maximum cross-sectional area
A_w	wetted area
c	specific heat of the model material
C_D	total drag coefficient
d	diameter of the model
h	enthalpy
K_1, K_2	constants of proportionality
M	Mach number
m	model mass
n	exponent in equation (5)
Q_{aero}	total aerodynamic heat transfer
ΔQ	energy added to calorimeter
\dot{q}_{av}	heat-transfer rate defined by equation (4)
\dot{q}_l	local heat-transfer rate

R_{∞}	Reynolds number based on free-stream properties, $\frac{\rho_{\infty} V_{\infty} d}{\mu_{\infty}}$
R_{ns}	Reynolds number based on properties behind a normal shock, $\frac{\rho_{ns} V_{ns} d}{\mu_{ns}}$
r	reference radius
St	Stanton number, $\frac{\dot{q}_{av}}{(h_{st} - h_w) \rho_{ns} V_{ns}}$
T_c	temperature of the calorimeter
T_m	temperature of the model
t	time
V	velocity
x	distance along the flight path
ρ	density of the air
μ	coefficient of viscosity
α	angle of attack

Subscripts

catch	conditions just prior to entering catcher
i	conditions prior to launch
L	launch conditions
ns	conditions behind normal shock
r	recovery conditions
st	stagnation conditions
w	wall (model surface) conditions
∞	free-stream conditions

TEST TECHNIQUE

Since the experimental technique presented in this report is new, it will first be described in general and then the more important features will be discussed in detail.

The test setup is shown schematically in figure 1. A model, held in a plastic holder called a sabot, is launched from a gun. The model, after being stripped of its sabot, enters the ballistic range and is photographed at spark shadowgraph stations while decelerating. The model scale, model material, air density, and range length are selected so that the model slows to a speed of a few hundred feet per second before entering the catcher. The model then pierces sheets of paper, decelerates to zero forward velocity, and falls through a paper funnel into a calorimeter where the total heat is measured.

As the model decelerates, a major portion of its kinetic energy heats the surrounding air via the strong bow shock wave; the remaining kinetic energy is delivered to the boundary layer via skin friction and to the model surface by conduction and convection. At the beginning of the flight, the rate of deceleration, and therefore the rate of energy loss, is high, causing a high heating rate. As the model progresses downrange, the deceleration and the heating rate to the model decrease. Shown in figure 2 are typical examples of a calculated heating-rate history, an integrated heating history, and a calculated velocity history for the case of a 1/4-inch aluminum hemisphere at sea-level conditions. The heat-transfer rate, \dot{q}_{av} , shown in this figure, is the surface-averaged heat-transfer rate. All of these curves have been normalized by an appropriate maximum value. It can be seen from this figure that the major portion of the heating occurs when the velocity is still relatively high. The experimental measurements were used to determine instantaneous heating rates from the variation of total heat transfer with model velocity.

TEST EQUIPMENT

Guns

Two different types of guns were used to span the velocity range covered by the present tests: a powder-gas gun for obtaining the data up to a velocity of 7,000 ft/sec and a single-stage shock-heated light-gas gun for extending the data to 11,000 ft/sec. Each gun had a smooth-bore launch barrel with a nominal inside diameter of 0.50 inch.

Models, Sabots, and Gas Seals

The geometry and dimensions of the models used in the present tests are shown in figure 3. The models are machined from solid 7075-T6 aluminum alloy. The surface finish was sufficiently smooth to maintain laminar flow, at least to

the model base. The diameters and material were selected to allow the model to decelerate at 1 atmosphere pressure from 11,000 ft/sec to about 500 ft/sec in the 200-foot length of the range. In figure 4 a typical model of each configuration is shown with its associated sabot.

Each sabot, in addition to its usual functions of supporting the model during the launch and providing a seal between model and launch barrel, was designed to act as a thermal protector against three sources of heating - barrel friction, compressed gas in front of the sabot, and driver gas behind the sabot. The protection provided by the sabot alone against the driver gas was found to be inadequate; the extreme pressure apparently forced hot gas down the parting planes of the sabot, causing severe heating of the model (see fig. 5(a) for a drawing of a sabot). This leakage was prevented by a separate gas seal behind the sabot, the one-piece polyethylene gas seal shown in figure 5(b). Additional heat protection consisting of several discs of 1 mil mylar was placed against the base of the models.

Pressurized Ballistic Range

The pressurized ballistic range is a 200-foot-long, 10-foot-diameter pressure vessel internally instrumented with conical-light shadowgraph stations at various intervals along the flight path. Firing times of the shadowgraph-station sparks are recorded with counter chronographs, so that the deceleration history of the model can be determined. The shadowgraph pictures also provide angle-of-attack history and flow visualization. Typical shadowgraphs of each of the models tested are shown in figure 6.

Catcher and Funnel

The catcher was designed to stop models flying at subsonic speed, intact and without appreciably altering their total heat content. The catcher consisted of 45-50 sheets of building paper (Federal specification UU-P-271-Type C), hung on a rack. Sheets were spaced about $3/4$ inch apart so the model could fall freely between any two sheets into the funnel.

The funnel was formed of heavy brown wrapping paper with steep sides and squared corners. The purpose of this design was to reduce the tendency of the model to spiral down the funnel, which would increase the transit time and permit additional heat loss from the model to the funnel and the air. The heat loss during transit through the catcher and funnel was small but measurable. A discussion of this loss is given in appendix A.

Calorimeter

The calorimeter employed was designed specifically for this application. A detailed description and the method of calibration are given in appendix B.

The unit shown in figure 7 consists of a thin silver cup into which the model drops, a large heat sink which absorbs the heat of the model and serves as a thermocouple cold junction, and a conduction path between the silver cup and the heat sink. The cup and the heat sink are each instrumented with 7 iron-constantan thermocouples. Six of the thermocouples from the heat sink are connected in series with six from the cup, forming a thermopile whose output is proportional to the temperature difference between the cup and the heat sink. This output, in millivolts, is recorded on a strip chart recorder. The remaining thermocouples, one in the cup and one in the heat sink, are used to record absolute temperatures.

Shown in figure 8 is a typical output signal from the calorimeter thermopile. Since, as discussed in appendix B, this signal represents the temperature difference, ΔT , between a heat source and a heat sink connected by a conduction path, the heat input, ΔQ , to the calorimeter is proportional to the area under the ΔT versus time curve; that is,

$$\Delta Q = K_1 \int_0^{\infty} \Delta T \, dt \quad (1)$$

where K_1 is a constant of proportionality. The constant K_1 was determined from prior calibration of the calorimeter and was found to be independent of model geometry, model orientation in the cup, and nonuniform temperature distribution in the model.

An electromechanical integrator was, for convenience, used to obtain the area under the temperature-time curve, its input signals being "picked off" the strip chart recorder. Measurements of heat inputs as low as 10^{-5} Btu were found to be possible with this equipment. The development of this highly sensitive and accurate calorimeter made the tests possible since, as will be noted in later sections, heat quantities to be measured in the tests were in the range from 0.001 to 0.01 Btu.

DATA REDUCTION AND ERROR ANALYSIS

Reduction of Total Heat-Transfer Data

The reduction of the total heat-transfer data proceeds from an energy balance. The thermal energy, ΔQ , added to the calorimeter by the model is obtained directly from the area under the ΔT versus time curve of the calorimeter and the calibration constant K_1 . This increment of energy, ΔQ , consists

of two parts, the energy due to aerodynamic heating, Q_{aero} , and the energy due to possible differences in the energy levels of the model and the calorimeter prior to launching of the model. The increment in energy, ΔQ , can be expressed in equation form, as

$$\Delta Q = Q_{aero} + mc(T_{m_i} - T_{c_i}) \quad (2)$$

where m is the mass of the model, c is the specific heat of the model material, and T_{m_i} and T_{c_i} are the prelaunch model and calorimeter temperatures, respectively. In equation (2) no extraneous sources of heat are assumed. This assumption was found to be good if proper precautions were taken. (See appendix A for the details of these precautions.) Solving equation (2) for Q_{aero} yields

$$Q_{aero} = \Delta Q - mc(T_{m_i} - T_{c_i}) \quad (3)$$

The last term on the right, which represents the correction for differences in energy levels of the model and calorimeter, was generally less than 10 percent of Q_{aero} . The temperature of the model was taken as the gun temperature prior to the launching, a satisfactory assumption if the model is allowed to come to thermal equilibrium with the gun. This was insured by loading the model into the gun at least one hour prior to launch.

Conversion of Total Heat-Transfer Measurements to Instantaneous Heating Rates

The total heat, determined from the calorimeter, transferred to the model during flight, Q_{aero} , may be further analyzed, by an integration technique, to obtain the instantaneous average heat-transfer rate over the surface as a function of velocity. The instantaneous average heating rate, \dot{q}_{av} , will be defined as

$$\dot{q}_{av} = \frac{1}{A_w} \int_{A_w} \dot{q}_l dA_w \quad (4)$$

where \dot{q}_l is the local heat-transfer rate, and A_w is the wetted area of the body. The functional relationship between \dot{q}_{av} , free-stream density, and velocity is assumed to be similar to the one discussed in reference 2. This relationship is

$$\dot{q}_{av} = K_2 \sqrt{\frac{\rho_\infty}{r}} V_\infty^n \quad (5)$$

where ρ_∞ is the free-stream density, r is a reference length (e.g., radius of curvature at the stagnation point), V_∞ is the flight speed, and K_2 and n are constants to be determined.

The total aerodynamic heat transfer to a model during a given trajectory can be expressed as

$$Q_{aero} = A_w \int_0^t \dot{q}_{av} dt \quad (6)$$

where t is the time of flight.

From the equation of motion, we obtain

$$dt = \left(\frac{-2m}{C_D A_c} \right) \frac{dV}{\rho_\infty V_\infty^2} \quad (7)$$

Equations (5), (6), and (7) may be combined as

$$Q_{aero} = \frac{-K_2 2m A_w}{\sqrt{\rho_\infty r} A_c} \int_{V_L}^{V_{catch}} \frac{V_\infty^{n-2}}{C_D} dV \quad (8)$$

Since the velocity history and drag coefficient are known, evaluation of the integral depends only on selection of n and K_2 to give a functional dependence of Q_{aero} on launch velocity which matches that recorded experimentally from test shots at different launch velocities. The procedure for selecting n and K_2 to obtain a best fit to the experimental data is given in appendix C.

The analysis described above works very well if both K_2 and n are constant or very nearly constant over the trajectory; however, this is true only for the case of near-zero angle of attack or where the heating rate is independent of the angle of attack and when the surface temperature is small compared to the recovery temperature. These conditions were found to be satisfied for that portion of the flight during which the major portion of the heating occurred.

Determination of Launch Velocity and Drag

Launch velocity.— The launch velocity (i.e., velocity at the muzzle of the gun) was deduced by extrapolation of velocities measured, at stations located 14 to 20 feet from the gun muzzle, back to the gun muzzle. This extrapolation was based on experimental drag coefficients and the equation of motion along the flight path, which in one form is

$$\frac{dV}{dx} = \frac{C_D A_c}{2m} \rho_\infty V_\infty \quad (9)$$

Drag.-- Equation (9) was used to deduce the drag data presented in the report from the velocity history obtained from the first seven shadowgraph stations. The drag coefficient, C_D , was assumed to be constant locally. Equation (9) was then integrated directly to yield

$$\ln V = \frac{A_c \rho_\infty}{2m} C_D x + \text{Constant} \quad (10)$$

The logarithm of the measured velocity, V , was plotted versus x and the local slope of this curve is proportional to C_D . The constant of proportionality, $A_c \rho_\infty / 2m$, is known. Extension of the curve (which, in general, is a straight line) back to the position of the gun muzzle gives the velocity of the model at launch.

Error Analysis

The accuracy of the total heat-transfer measurements depends upon the accuracy of the calorimeter system and the magnitude of extraneous heat sources and sinks. The calorimeter has a maximum error of ± 3 percent of the total heat-transfer measurement (determined from calibration). Several sources of extraneous heating were considered; listed below are the most significant ones along with their estimated size.

Leakage of hot driver gas to model	+0% -2% of Q_{aero}
Heating and/or cooling in the catching process	$\pm 1 \times 10^{-4}$ Btu

The method of estimating the size of these errors can be found in appendix A. The sum of the estimated errors in the total heat measurements is listed below for three different velocities.

	Error range, percent	Launch velocity	
Total aerodynamic heating, Q_{aero}	+13 -15	5,000	} Hemisphere and 60° blunted cone
	+8 -10	7,000	
	+6 -8	10,000	

Because of the method of data reduction used, it is difficult to estimate the accuracy of the heating rates, \dot{q}_{av} . The maximum expected error could be larger than the maximum error in the total heat-transfer measurements. As will be shown later, the agreement between the heating rates obtained by the present technique and with well-established theory, for the case of a hemisphere, which is for all practical purposes a proof configuration, is near the maximum error in the total heating measurements. It should be pointed out that one should be careful in extrapolating the heating results outside of the range of launch velocities considered.

The estimated accuracy of measured drag coefficient and launch velocity is 1 percent.

TEST CONDITIONS

All of the tests of the present report were conducted at sea-level atmospheric conditions. The test conditions are listed in table I. Since Reynolds number and angle of attack can have a large influence on heat transfer, these quantities will be discussed below.

Reynolds Number

Because the tests were made at constant density over deceleration-type trajectories, the free-stream Reynolds number, R_∞ , varied directly with the instantaneous velocity as follows:

$$R_\infty = 6.25 V_\infty d \times 10^3 \quad (11)$$

where V_∞ is the flight velocity in feet per second, and d is the reference diameter in feet. At a muzzle velocity of 11,000 ft/sec and a diameter of 0.02083 ft (0.250 inch), the Reynolds number is approximately 1.43 million.

One form of the Reynolds number, which is useful in correlating heat-transfer results, is very nearly constant over the major portion of the trajectory, that is, R_{ns} , based on the properties behind a normal shock and a reference diameter. In the present tests R_{ns} varied between 0.23 million and 0.29 million for the hemisphere and between 0.18 million and 0.23 million for the 60° blunted cone, for the range of launch velocities considered in this report.

Angle of Attack

In ballistic testing the angle of attack cannot be accurately controlled, but depends on random factors such as the separation interactions of the model and sabot. For present purposes, model-sabot combinations were sought which yielded small initial angles of attack. This was achieved for the case of the 60° blunted cone and was partially successful for the hemisphere. (The hemisphere was a less critical case because the heat transfer is nearly independent of angle of attack, at least for angles less than 15°.)

RESULTS AND DISCUSSION

Heat-Transfer Results

Because the experimental technique used to obtain the data in this report is new, the heat-transfer results will be presented in the following order. First, the measured total heat-transfer data will be presented. Second, the data for the hemisphere, which is considered to be a test case for the new technique, will be discussed and compared to established theory. Third, the remainder of the results will be reduced to surface average heating rates and put in dimensionless form.

Total heat transfer.- Figure 9 shows the total heat Q_{aero} transferred to the various models tested as a function of launch velocity. These results are also tabulated in table I.

Comparison of the hemisphere results with theory.- Upon applying the data reduction method described earlier to the total heat-transfer results and using experimental drag coefficients, to be presented later, we obtain heat-transfer rates in the form

$$\dot{q}_{av} = K_2 \sqrt{\frac{\rho_{\infty}}{r}} V_{\infty}^n \quad (5)$$

where the values of K_2 and n were determined from the data of the present tests and are listed in table II.

Shown in figure 10 are the heating-rate results for the hemisphere. For comparison, theoretical calculations at Mach numbers 4 and 6 by the method of Stine and Wanless (ref. 3) are presented. These theoretical results are indicated by the circled points. Further theoretical calculations were made using the stagnation-point results of Fay and Riddell (ref. 4) and the distributions from the method of reference 3. Calculation for several points allowed a curve to be drawn through the speed range shown. (All theoretical calculations are for the case of zero base heat transfer.) It can be seen that the agreement with theory is very good. The differences are no greater than 19 percent and in the case of the Fay and Riddell stagnation-point plus Stine and Wanless distribution, the neglected base heating is in a direction to improve the agreement. Also shown is the stagnation-point heat-transfer rate calculated by the method of reference 4 upon which the second theoretical estimates were based.

Fraction of kinetic energy loss converted to aerodynamic heat input to model.- A direct comparison of the total heat absorbed by the various configurations is not meaningful because the configurations have different values of the ballistic parameter ($m/C_p A_c$). It can be anticipated, however, that to a first order of approximation the heat absorbed by a given configuration, decelerating between fixed velocity limits, should vary directly with the kinetic energy loss of the model. The total aerodynamic heat input divided by the kinetic energy at launch, which is approximately equal to the kinetic energy loss, is plotted in figure 11(a) as a function of launch velocity. Here it can be

seen that the configuration with higher total drag coefficient, the hemisphere, receives a smaller fraction of the available kinetic energy as heat transferred to the vehicle. This is consistent with arguments advanced by Allen and Eggers, reference 5. The unfavorable trend of the increased fraction of kinetic energy resulting in heating of the 60° blunted cone is due to the fact that the drag coefficient is decreasing with increasing velocity.

In figure 11(b) are shown the same basic results normalized by the square root of the Reynolds number based on flow properties behind the normal shock. Plotted in this manner the data are more easily used to calculate heating loads at other test conditions. The results show the same basic trends as figure 11(a).

Comparison of heat-transfer rates.- The test results in the form of instantaneous average heat-transfer rates are plotted in figure 12, referenced to the cross-sectional area, as a function of velocity. Considering the extreme variations in local heat transfer it is surprising to note how closely these curves are grouped. These results follow the same trend exhibited by the fraction of kinetic energy appearing as heat transferred to the vehicle - namely, the lower the drag coefficient, the higher the heating load. It is further noted that the velocity dependence, the exponent n , is almost identical for the hemisphere and the 60° blunted cone. At first glance this would seem inconsistent with the results in figure 11, which show a different velocity dependence for the two configurations. The explanation is that the C_D of the hemisphere is independent of velocity, but the C_D of the 60° blunted cone decreases approximately as $1/V$. The effect of this on the total heat transferred to the model may be seen by referring to equation (8).

When considered in the context of equation (5), the slopes of the curves in figure 12 are equal to the exponent n . The larger the value of n , the faster the heating rate increases with velocity.

Dimensionless heat-transfer parameter.- The heat-transfer rates were reduced to the dimensionless form, average Stanton number, St , defined as

$$St = \frac{\dot{q}_{av}}{(h_r - h_w)\rho_{ns}V_{ns}} \quad (12)$$

where the subscript ns refers to conditions behind the normal shock, and h_r and h_w are the recovery and wall enthalpies, respectively. For the case of heating rates over blunt bodies, h_r ranges from being equal to stagnation enthalpy, h_{st} , at the stagnation point, to some large fraction of h_{st} at points downstream of the stagnation point (e.g., $h_r = 0.935 h_{st}$ at the shoulder of a hemisphere, ref. 6). Since these fractions are always large, for simplicity, we chose $h_r = h_{st}$.

The model surface temperature, and therefore h_w , is continually changing during flight. It starts out uniform and equal to gun temperature before launch and it rises very rapidly at the high speeds, then diminishes as the heating rate decreases with decreasing velocity. A check of the model temperature distribution near the surface was made using an electrical heat flow analog (ref. 7).

The surface temperature was found to be at all times low compared to the recovery temperatures, as was borne out by the fact that no indications of melting of the model surface were observed on recovered models. Therefore the cold-wall assumption was used for h_w ; that is, $h_w = h_{mi}$.

A remark can also be made concerning the uniformity of wall temperature in the direction of flow. The temperature distribution from the analog simulation indicated that the departure from isothermal wall conditions is small compared to the recovery temperature. Therefore the results of the present tests can be considered as good approximations to isothermal wall heat-transfer data.

Shown in figure 13 is the product of Stanton number, based on maximum cross-sectional area, and the square root of the Reynolds number, based on properties behind the normal shock, as a function of stagnation enthalpy for the various configurations at zero angle of attack. It can be seen that plotted in this manner the present test data appear to correlate very well and there appear to be only small changes in $St\sqrt{R_{ns}}$ with stagnation enthalpy.

Drag Data

Knowledge of the drag history was essential to the reduction of the total heat-transfer data. In figure 14 the drag coefficients of the configurations tested are shown plotted as a function of Mach number. These data were obtained from the local slopes of the $\ln V$ versus x curves and, hence, give drag coefficients at several Mach numbers. In this figure are the results for the hemisphere and the 60° blunted cone. These results cover the speed range from subsonic to a Mach number of about 4.5 and show the characteristic transonic C_D hump. Comparison shown in this figure of the present results to earlier free-flight results for larger models and higher Mach numbers shows very good agreement.

SUMMARY OF RESULTS

A new technique for obtaining experimental heat-transfer data at high speeds has been presented. The technique, once developed, is very simple to use. Furthermore, it has the potential of being relatively accurate compared to other heat-transfer measurement techniques. The heat-transfer results for a hemisphere were compared with theory and were found to be in very good agreement. A disadvantage of the technique is that, in some cases, many data points are required to obtain the desired results - for example, where heat transfer is a strong function of angle of attack.

Possible applications of the technique not considered in this report are determination of heat transfer in gases other than air and measurement of heat absorbed by ablating bodies.

The heat-transfer characteristics of the two blunt bodies measured by this technique showed that the portion of the initial kinetic energy which appears as heat transferred to the model was highest for the model with lowest drag coefficient. A similar trend was evident for the heat-transfer rates based on the maximum cross-sectional area. The effect of stagnation-point enthalpy on the heat-transfer parameter, $St \sqrt{R_{ns}}$, was small.

Ames Research Center

National Aeronautics and Space Administration

Moffett Field, Calif., April 11, 1963

APPENDIX A

EXTRANEOUS HEAT SOURCES

As noted in the text, there are several extraneous heat sources and sinks which could give rise to errors in the aerodynamic heating data, including:

1. Heating due to shock-heated gases in front of the model while the model is traversing the launch tube.
2. Heating caused by propellant leaking through sabot to model.
3. Heat loss due to long subsonic flight.
4. Heating and/or cooling due to catcher and funnel.

Items 1 and 2 were discussed in some detail in the text; however, a brief description of the extent to which these sources of heat were eliminated is included here. The complete enclosure of the model by the sabot, along with the partial evacuation of the launch tube, was thought to completely eliminate heating resulting from item 1.

The heating resulting from item 2 was as high as 100 percent of Q_{aero} when no obturation cup was used. The effectiveness of the obturation cup in reducing this heating was ascertained from several test shots with gas seals of various designs. (Several shots with various length gas seals were fired at the same launch velocity; when the heat input was plotted versus the length of gas seal, the curve appeared to approach a constant value which was considered to be the case of zero heating by gun gases.) The obturation cup used for all tests included in this report appeared to reduce this heating to about 7 or 8 percent of Q_{aero} . Additional heat protection, consisting of thin sheets of mylar placed over the base of the models with flat bases, appeared to further reduce this heating to a couple of percent of Q_{aero} .

Heat is lost from the model during the relatively "long" subsonic flight time to the catcher of approximately 0.1 second. The electrical heat flow analog computer at Ames was programmed to represent the thermal properties of the hemisphere model and the heat transfer to the model. The model was then "flown" from 10,000 feet per second to 1,000 feet per second and then the front face inputs were switched to represent cooling to the atmosphere (i.e., $h_r = h_{\infty}$). In 0.1 second of "flight" two percent of the model's total heat was lost. Since the average cooling rate during subsonic flight is numerically less than the 1,000 feet per second cooling rate which was employed, it can be concluded that the subsonic flight heat losses are negligible. At subsonic flight times longer than 0.2 second the cooling would increase rapidly; therefore the catch should be made at as high a subsonic speed as possible. In the present tests, catches were made between 300 and 800 feet per second.

The heating of the model in passing through the catcher and funnel combination is from three sources: deformation of the model; friction between model and paper; and conduction between model, paper, and air. The models were examined under a microscope after they had penetrated the sheets of paper and no sign of deformation was evident. It was therefore felt that the heating due to deformation was negligible. The other two sources of heat transfer were difficult to analyze, and since the models enter the catcher with kinetic energy of the same order of magnitude as the total aerodynamic heating, this extraneous heating could be large if a substantial fraction of this energy were converted to heat in the model.

To assess the amount of extraneous heating in the catcher-funnel, a compressed air gun was built so that the major portion of the barrel passed through a temperature-controlled oven. This gun was set up to fire into the catcher-funnel-calorimeter combination. Two series of tests were conducted with a 1/4-inch aluminum sphere used as the test model. In one, the model was launched cold (i.e., at the same temperature as the catcher) to minimize conduction effects in the catcher. Launches were made at various velocities and therefore various numbers of sheets of catcher paper were penetrated. The measured heat input increased significantly with the number of sheets penetrated; it was, however, less than one-thirtieth of the available kinetic energy. The second test was conducted with the model heated to between 35° to 40° F above the temperature of the catcher. In this case the difference in thermal energy (i.e., measured minus calculated) at first decreased and then increased with increasing number of sheets penetrated (increasing velocity); it was zero after about 28 sheets were penetrated. This indicates that at first the heating in the catcher is controlled by conduction losses and finally friction heating gains control and the heating increases. The maximum errors resulting from these effects in the actual heating experiments occurred at the lower speeds where they were as high as ± 10 percent of the total aerodynamic heating ($\pm 1.0 \times 10^{-4}$ Btu).

Two comments are in order as to the catcher-funnel errors. First, the paper used in this catcher was the only material tried. It is not very likely that it is the optimum from a heat-transfer standpoint. Secondly, the simple experiment indicated that even the 10-percent error could be partially eliminated if, with a setup similar to the one described, the heating in the catcher were determined carefully for each configuration.

APPENDIX B

THE CALORIMETER AND ITS CALIBRATION

Basically, the calorimeter consisted of a thin silver cup into which the model was dropped, a heat sink to dissipate the heat, and a controlled conduction path between the cup and heat sink. Each of these elements had a particular function and in some cases more than one function. A quarter-sectional view of the calorimeter can be found in figure 7.

Silver Cup

The silver cup acted as a receiver and transducer for the hot model. Since the electrical signal representing model total heat was obtained from a thermopile attached to the cup, it was important to keep the heat capacity of the cup very low and the diffusivity high. Thus the silver cup had to be as small and as thin (approximately 0.003 in. wall thickness) as possible so it could come to an equilibrium temperature with the hot model very rapidly and also have a fairly high temperature with a small heat input. The cup was instrumented with a thermopile consisting of 7 iron-constantan thermocouples on the bottom exterior. Six of these were connected in series with 6 reference junctions located in the heat sink. The seventh thermocouple was used to determine absolute temperatures.

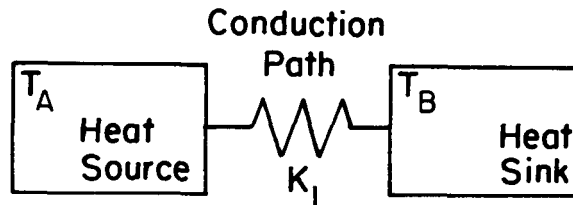
Heat Sink

The heat sink was constructed of two large blocks of phosphor bronze. The silver cup was suspended in a cavity in the lower block. Also buried in the lower portion of the lower block were 7 more iron-constantan thermocouples which utilize the heat sink as a constant temperature reference mass. The purpose of two large blocks was to provide a sufficiently large heat capacity so that the temperature level did not change more than a few thousandths of a degree during a shot and while temperatures were being recorded. This was necessary because the heat sink was used as a reference temperature for the 6 iron-constantan thermocouples. The upper block served to cover the cavity where the silver cup was suspended. The model entered the cup through a conical hole in the upper block. This hole was lined with a low conductivity plastic to minimize any heat transfer due to contact with the model as it dropped through to the cup.

Conduction path.— The suspension system for the cup also acted as the controlled conduction path between the cup and the heat sink. The conduction path consisted of three small thin support arms made of low conductivity epoxy resin. These were fastened between the upper lip of the cup and the rim of the cavity. The cross section of these supports was made so that the major portion of the heat from the hot model would be transferred to the heat sink in about 10 to 15 minutes. It was necessary to use very fine thermocouples (0.001-inch

diameter wire) on the cup to minimize their heat capacity and the conductivity between the cup and the heat sink. The excess volume of the cavity was filled with foamed plastic so that there would be no free convective heat transfer from the cup.

With the calorimeter constructed as described above, the measuring of the heat transfer can be expressed schematically as shown in sketch (a).



Sketch (a)

It is obvious from this sketch that the heat transfer from source to sink is as follows:

$$\frac{dQ}{dt} = K_1 [T_A(t) - T_B] \quad (B1)$$

thus

$$Q \equiv \Delta Q = K_1 \int_0^t [T_A(t) - T_B] dt \quad (B2)$$

Energy added
to calorimeter
via model

The output of the thermopile is proportional to the instantaneous temperature difference $T_A - T_B$ and is fed into an electromechanical integrator which solves equation (B2), yielding $\Delta Q/K_1$.

Calibration of the Calorimeter

The calorimeter was calibrated to determine the constant K_1 and to determine the effects of several variables on K_1 .

Basically, the calibration setup consisted of an oven suspended over the calorimeter. The model was placed in the oven, allowed to come to some known steady-state temperature, and dropped into the calorimeter. The integrated output, $\Delta Q/K_1$, of the thermopile was then read and plotted versus the calculated energy placed into the calorimeter via the hot model. (There was a radiation

shield between the oven and calorimeter at all times except during the dropping of the model.) This process was repeated at various oven temperatures. The plot of calculated heat input versus integrated values of $\Delta Q/K_1$ resulted in a straight line, the slope of which was the value of K_1 . The calibrations were repeated with variations of model geometry, model orientation in cup, model material, and nonuniform temperatures in the model. The value of K_1 was found to be constant within ± 3 percent over a range of thermal energies from 0.5×10^{-3} to 10×10^{-3} Btu. The model geometries for these calibrations were the two configurations of the present test and a 1/4-inch aluminum sphere. Most of the models were aluminum; however, several preliminary calibrations using a 1/4-inch Teflon hemisphere gave essentially the same results. The condition of nonequilibrium temperature distribution in the model was simulated by dropping two models at the same time but with different temperatures. Here again the agreement was well within the 3 percent.

APPENDIX C

REDUCTION OF THE TOTAL HEAT-TRANSFER DATA TO HEAT-TRANSFER RATES

The total heat absorbed by a nonablating vehicle in decelerating flight is given by equation (8) of the text as

$$Q_{aero} = \frac{-K_2 2m A_R}{\sqrt{\rho_{\infty} r} A_c} \int_{V_L}^{V_{catch}} \frac{V^{n-2}}{C_D} dV \quad (C1)$$

For the case of constant drag coefficient, equation (C1) can be integrated directly to give

$$Q_{aero} = \frac{K_2 2m A_R}{\sqrt{\rho_{\infty} r} A_c C_D (n-1)} \left(V_L^{n-1} - V_{catch}^{n-1} \right) \quad (C2)$$

In all cases the launch velocity is much greater than the catch velocity and the value of n , as determined by theory and substantiated experimentally, is usually about 3; therefore,

$$V_L^{n-1} \gg V_{catch}^{n-1}$$

and equation (C2) reduces to

$$Q_{aero} = \frac{K_2 2m A_R}{\sqrt{\rho_{\infty} r} A_c C_D (n-1)} V_L^{n-1} \quad (C3)$$

If equation (C3) is physically realistic, we see that the total aerodynamic heating should be a power-law function of the launch velocity; therefore a plot of Q_{aero} versus launch velocity on a logarithmic plot results in a straight line, the slope of which is equal to the exponent $(n-1)$, and the constant K_2 is the value of Q_{aero} at the one-foot-per-second intercept. Figure 9 shows that the data obtained do fall in an approximately straight line. A systematic method of applying equation (C1) which allows variation in C_D and is a least squares fit to the available data was therefore developed as follows.

Least Squares Analysis

In the least squares analysis the model velocity was assumed to be known exactly. The sum of the residuals σ can be written as

$$\sigma = \sum \left(Q_{\text{aeroexp}} - \frac{K_2 2m A_R}{\sqrt{\rho_\infty r} A_c} \int_{V_L}^{V_{\text{catch}}} \frac{v^{n-2}}{C_D} dv \right)^2 \quad (C4)$$

where the subscript exp refers to the experiment, and the summation extends over all the experimental points. The derivative of equation (C4) with respect to K_2 set equal to zero yields the value of K_2 for a particular n which minimizes the sum of the residuals for that value of n .

$$\frac{d(\sigma)}{dK_2} = 2 \sum \left(Q_{\text{aeroexp}} - BK_2 \int_{V_L}^{V_{\text{catch}}} \frac{v^{n-2}}{C_D} dv \right) B \int_{V_L}^{V_{\text{catch}}} \frac{v^{n-2}}{C_D} dv = 0 \quad (C5)$$

where

$$B = \frac{2m}{\sqrt{\rho_\infty r}} \frac{A_R}{A_c}$$

Thus, the best fitting value of K_2 is given by

$$K_2 = \frac{\sum Q_{\text{aeroexp}} B \int_{V_L}^{V_{\text{catch}}} \frac{v^{n-2}}{C_D} dv}{\sum \left(B \int_{V_L}^{V_{\text{catch}}} \frac{v^{n-2}}{C_D} dv \right)^2} \quad (C6)$$

This procedure was applied for several trial values of n and the corresponding sums of the residuals were plotted versus n . The value of n at the minimum of this curve along with the corresponding value of K_2 was selected as the best fit to the data. This graphical selection is equivalent to taking the derivative of equation (C4) with respect to n setting it equal to zero and solving that equation and (C5) simultaneously for K_2 and n ; the graphical method, however, is simpler.

REFERENCES

1. Yee, Layton, Bailey, Harry E., and Woodward, Henry T.: Ballistic Range Measurements of Stagnation-Point Heat Transfer in Air and in Carbon Dioxide at Velocities up to 18,000 Feet Per Second. NASA TN D-777, 1961.
2. Chapman, Dean R.: An Approximate Analytical Method for Studying Entry Into Planetary Atmospheres. NACA TN 4276, 1958.
3. Stine, Howard A., and Wanlass, Kent: Theoretical and Experimental Investigation of Aerodynamic-Heating and Isothermal Heat-Transfer Parameters on a Hemispherical Nose With Laminar Boundary Layer at Supersonic Mach Numbers. NACA TN 3344, 1954.
4. Fay, J. A., and Riddell, F. R.: Theory of Stagnation Point Heat Transfer in Dissociated Air. Jour. Aero. Sci., vol. 25, no. 2, Feb. 1958, pp. 73-85, 121.
5. Allen, H. Julian, and Eggers, A. J., Jr.: A Study of the Motion and Aerodynamic Heating of Ballistic Missiles Entering the Earth's Atmosphere at High Supersonic Speeds. NACA Rep. 1381, 1958. (Supersedes NACA TN 4047).
6. Jackson, Mary W., and Czarnecki, K. R.: Boundary-Layer Transition on a Group of Blunt Nose Shapes at a Mach Number of 2.20 NASA TN D-932, 1961.
7. Neel, Carr B.: Cooling of Structures in High Speed Flight. North Atlantic Treaty Organization Advisory Group for Aeronautical Research and Development. AGARD Rep. 210, Oct. 1958.
8. Seiff, Alvin, Sommer, Simon C., and Canning, Thomas N.: Some Experiments at High Supersonic Speeds on the Aerodynamic and Boundary-Layer Transition Characteristics of High-Drag Bodies of Revolution. NACA RM A56IO5, 1957.

TABLE I.- TEST CONDITIONS AND TOTAL HEAT-TRANSFER RESULTS

Test conditions						Test result			
Run	Configuration	Ambient pressure, psia	Ambient temp., °F	Model temp. prior to launch, °F	Model weight, grams	V _L , ft/sec	Q _{aero} × 10 ³ , Btu	Sheets penetrated	α _{RMS} , deg
365	<div style="display: flex; align-items: center; justify-content: center;"> <div style="text-align: center;">Hemisphere</div> <div style="margin: 0 10px;">↓</div> <div style="text-align: center;">60° blunted cone</div> </div>	14.75	78.2	77.9	0.1868	10,200	5.32	27	Not measured
394		14.89	74.7	70.8	.1874	7,780	3.62	20	< 4
395		14.85	77.4	72.3	.1875	11,000	6.78	28	< 10
397		14.85	81.8	79.7	.1869	9,610	5.15	25	< 15
398		14.74	74.7	75.4	.1871	5,730	1.74	18	< 8
400		14.77	72.3	70.2	.1851	5,760	1.71	18	< 11
402		14.85	63.7	69.0	.1870	4,290	0.904	21	< 11
407		14.76	67.1	66.3	.1867	9,630	4.76	59	< 14
429		14.74	66.4	63.3	.0841	9,230	3.71	13	< 5
430		14.74	66.5	65.2	.0819	9,620	3.91	15	< 5
463		14.89	56.5	51.1	.0824	6,900	1.66	13	< 5
464		14.79	65.6	55.3	.0822	5,600	1.06	9	< 5

TABLE II.- HEATING-RATE RESULTS

Configuration	Ref. area	Ref. radius	α _{RMS}	K ₂	n
Hemisphere 60° blunted cone	Front face wetted	Radius of cross section	< 15	5.85 × 10 ⁻⁹	3.051
			< 5	5.60 × 10 ⁻⁹	3.065

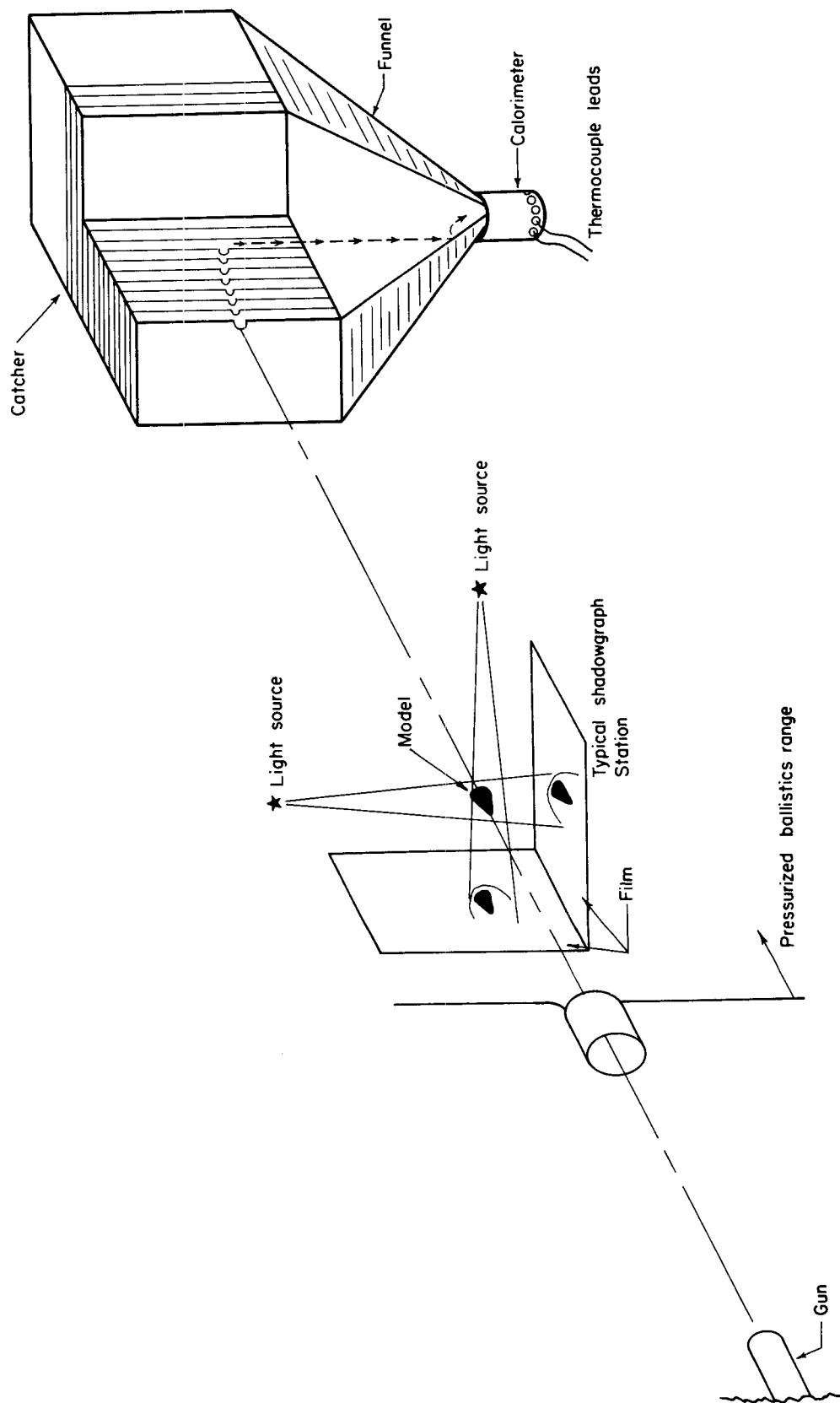


Figure 1.- Schematic drawing of test setup.

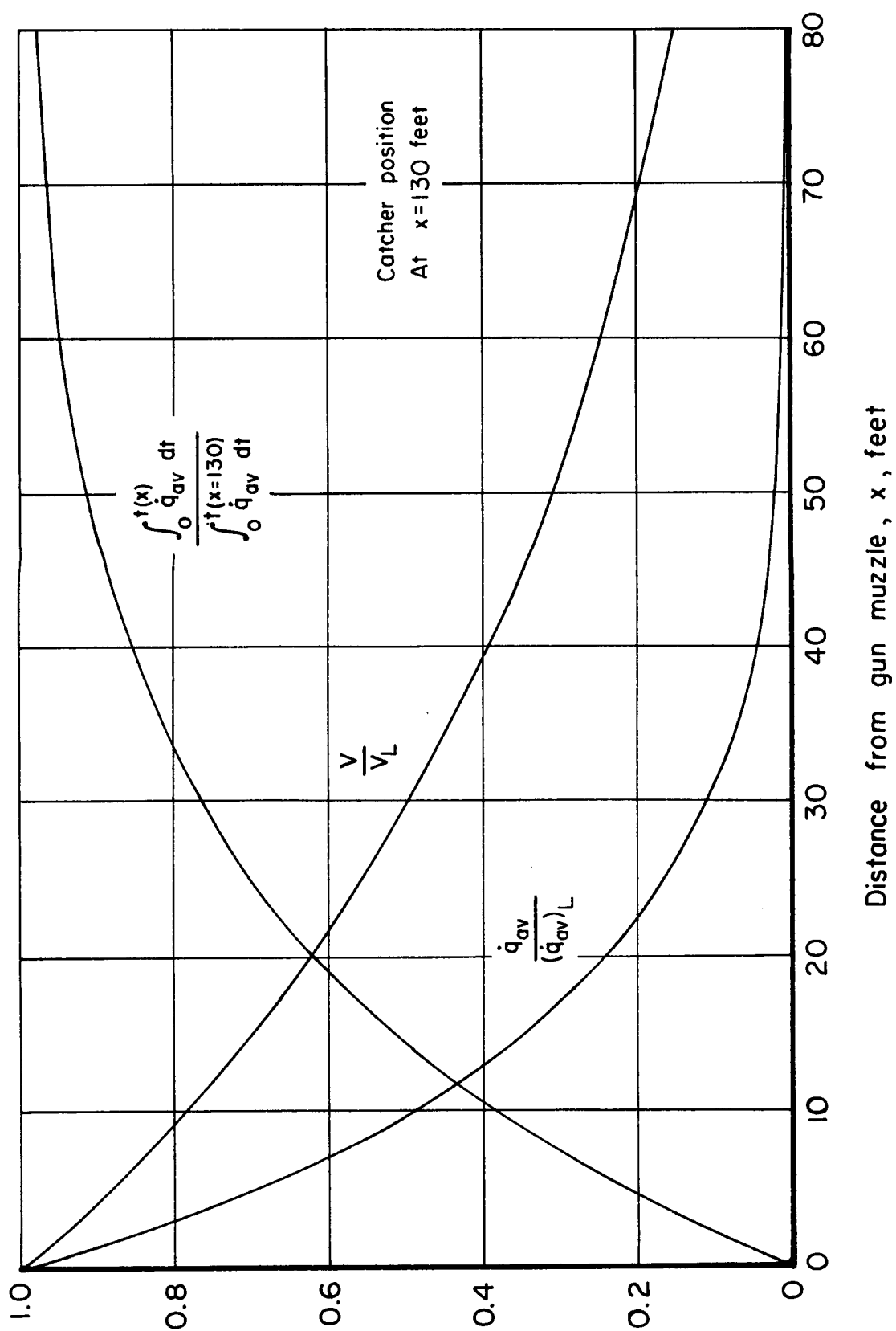
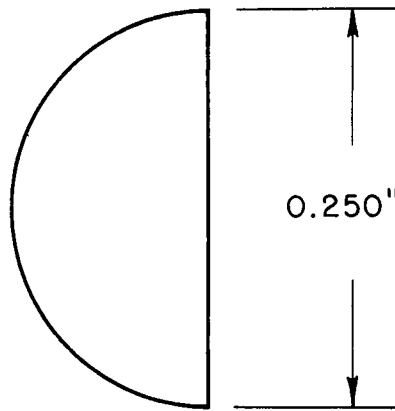
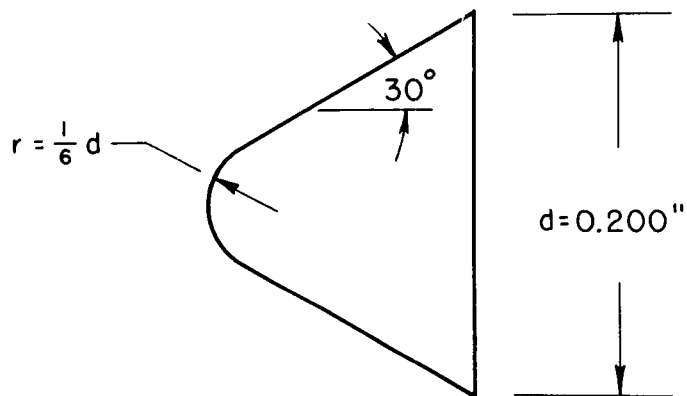


Figure 2.- Typical variations in heating and velocity with distance from the gun.

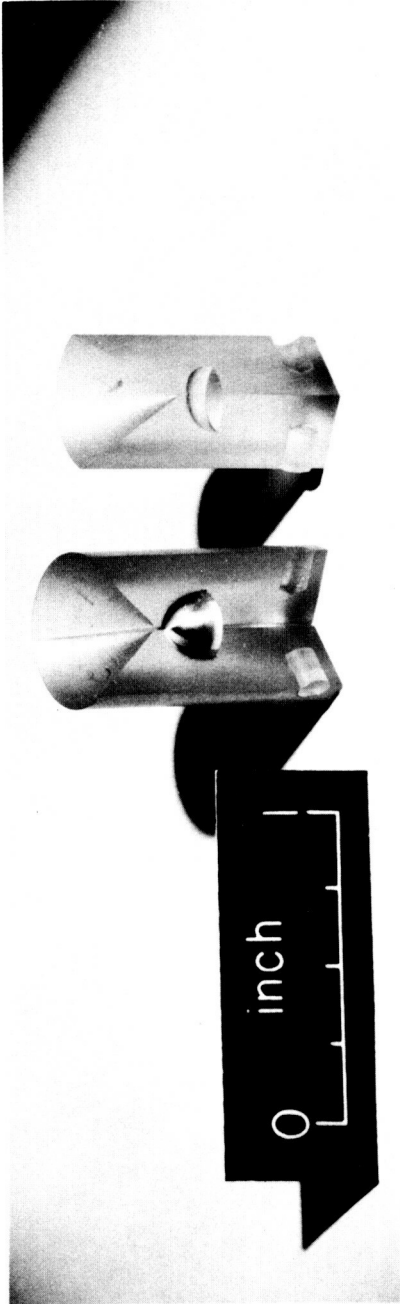


Hemisphere



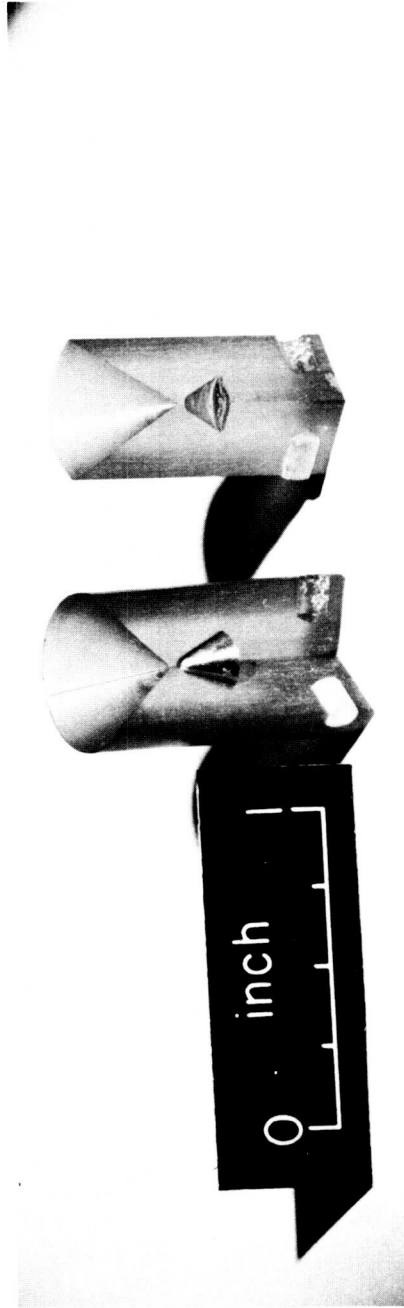
60° blunted cone

Figure 3.- Test configurations.



A-28919

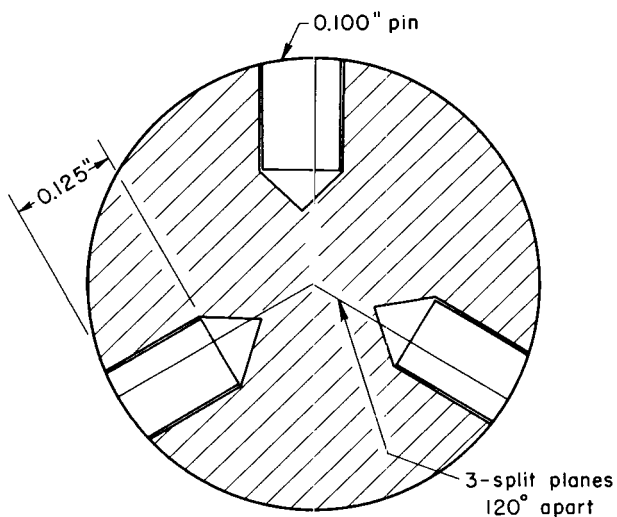
Hemisphere



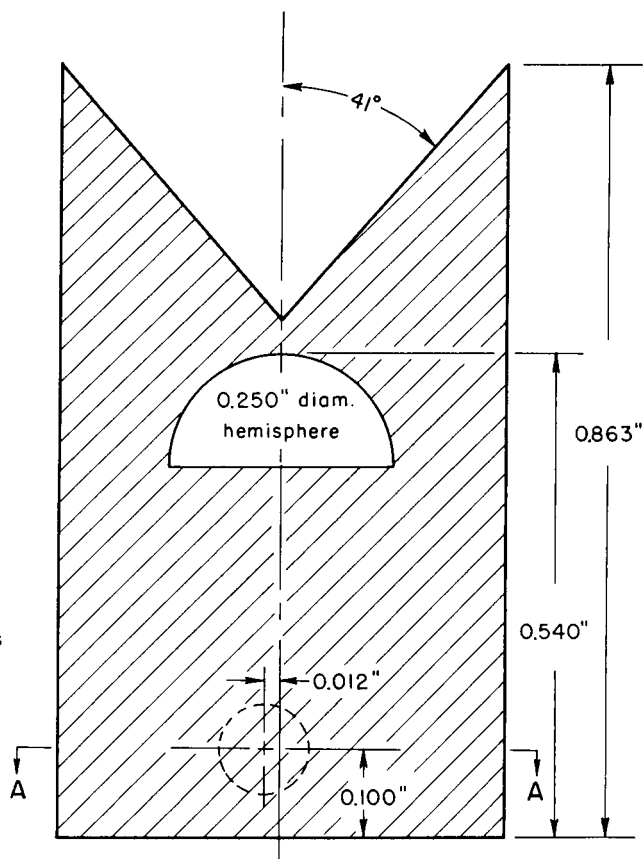
A-28918

60° blunted cone

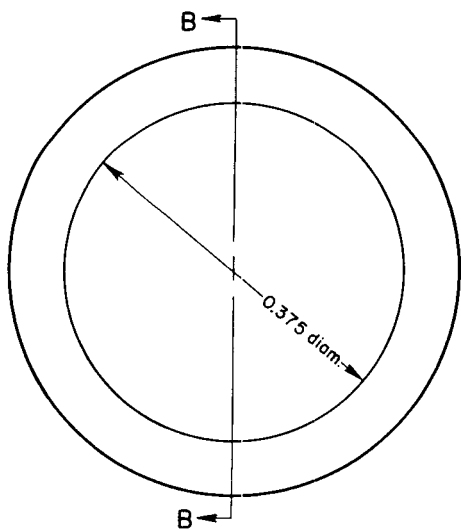
Figure 4.- Photographs of models and sabots.



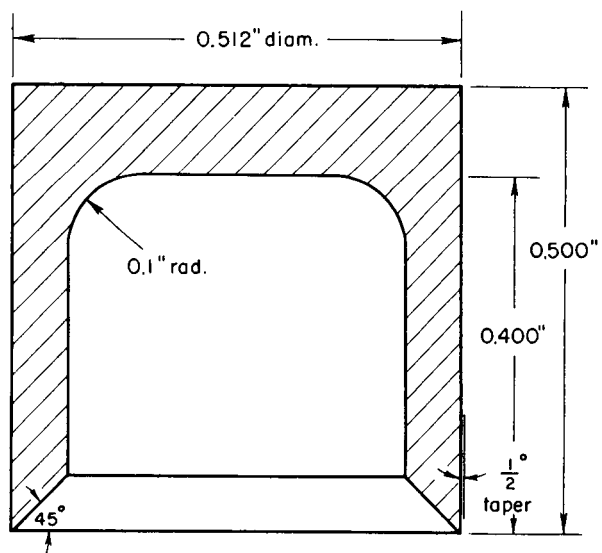
Section A-A
Material: Lexan



(a) Typical sabot



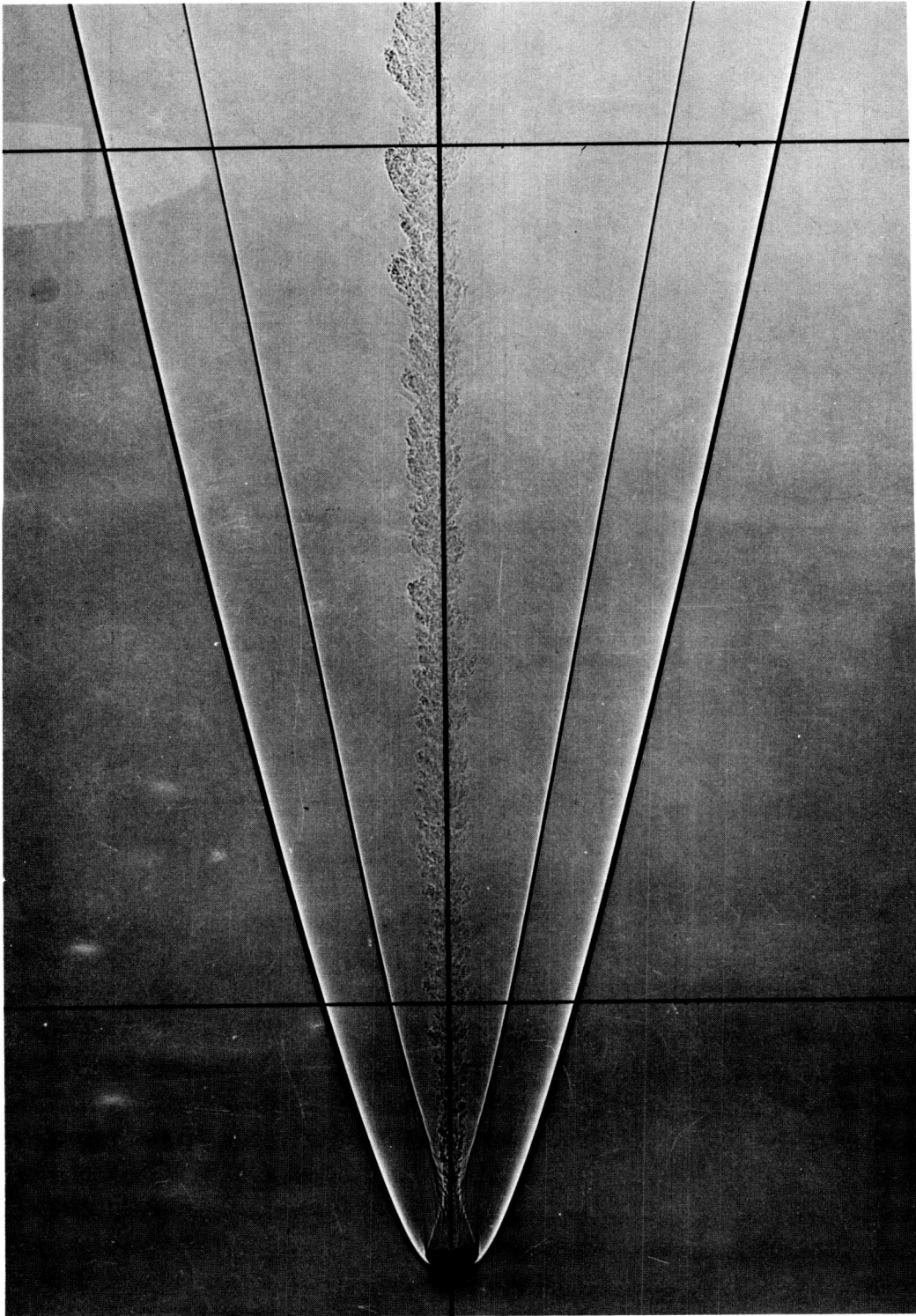
Material: Polyethylene



Section B-B

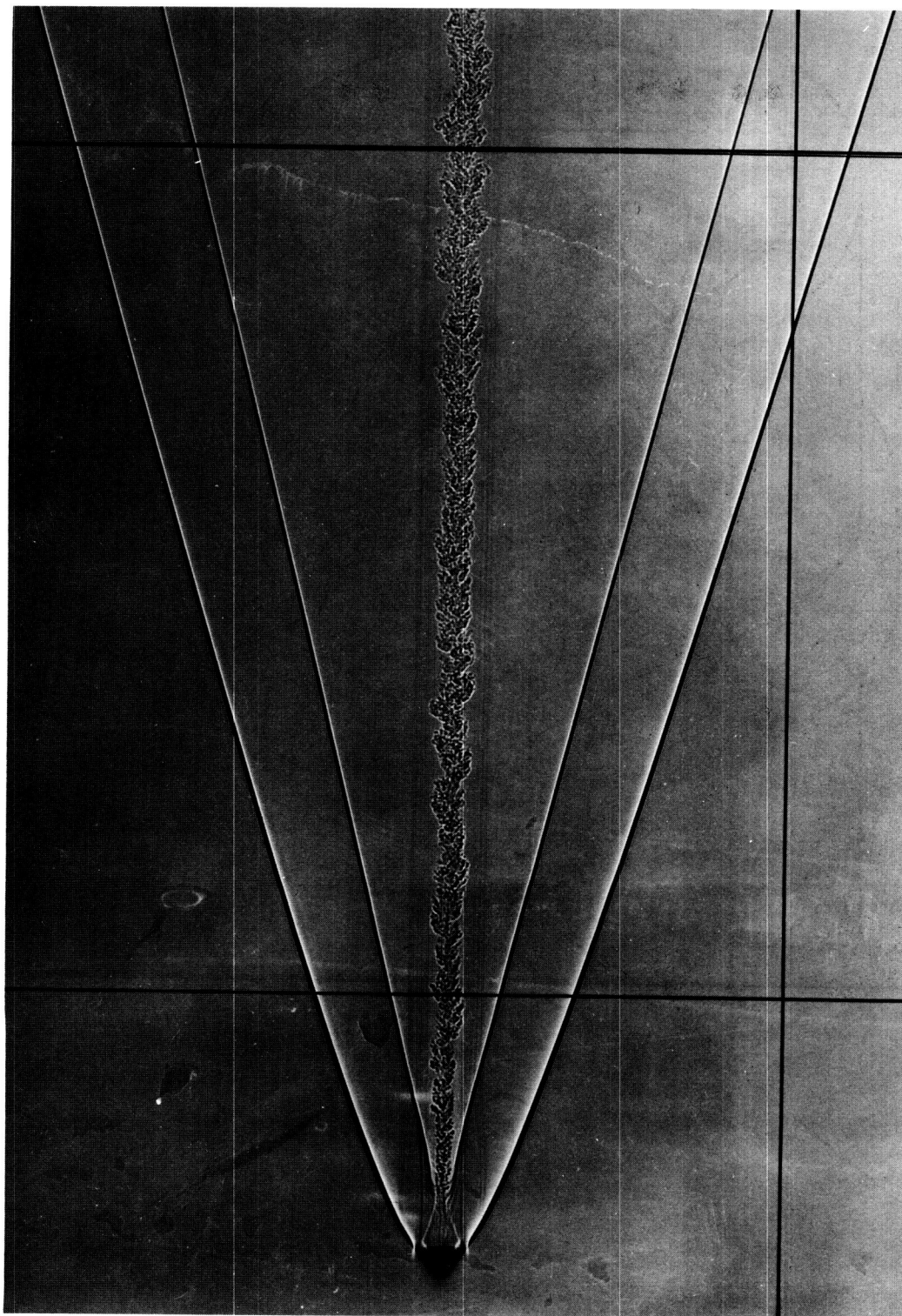
(b) Gas seal

Figure 5.- Sectional drawing of a typical sabot and gas seal.



(a) Hemisphere; $V_{\infty} = 5,770$ ft/sec, $P_{\infty} = 0.75$ million.

Figure 6.- Typical shadowgraphs of models flying at small angles of attack.



(b) 60° blunted cone; $V_\infty = 4,600$ ft/sec, $R_\infty = 0.60$ million.

Figure 6.- Concluded.

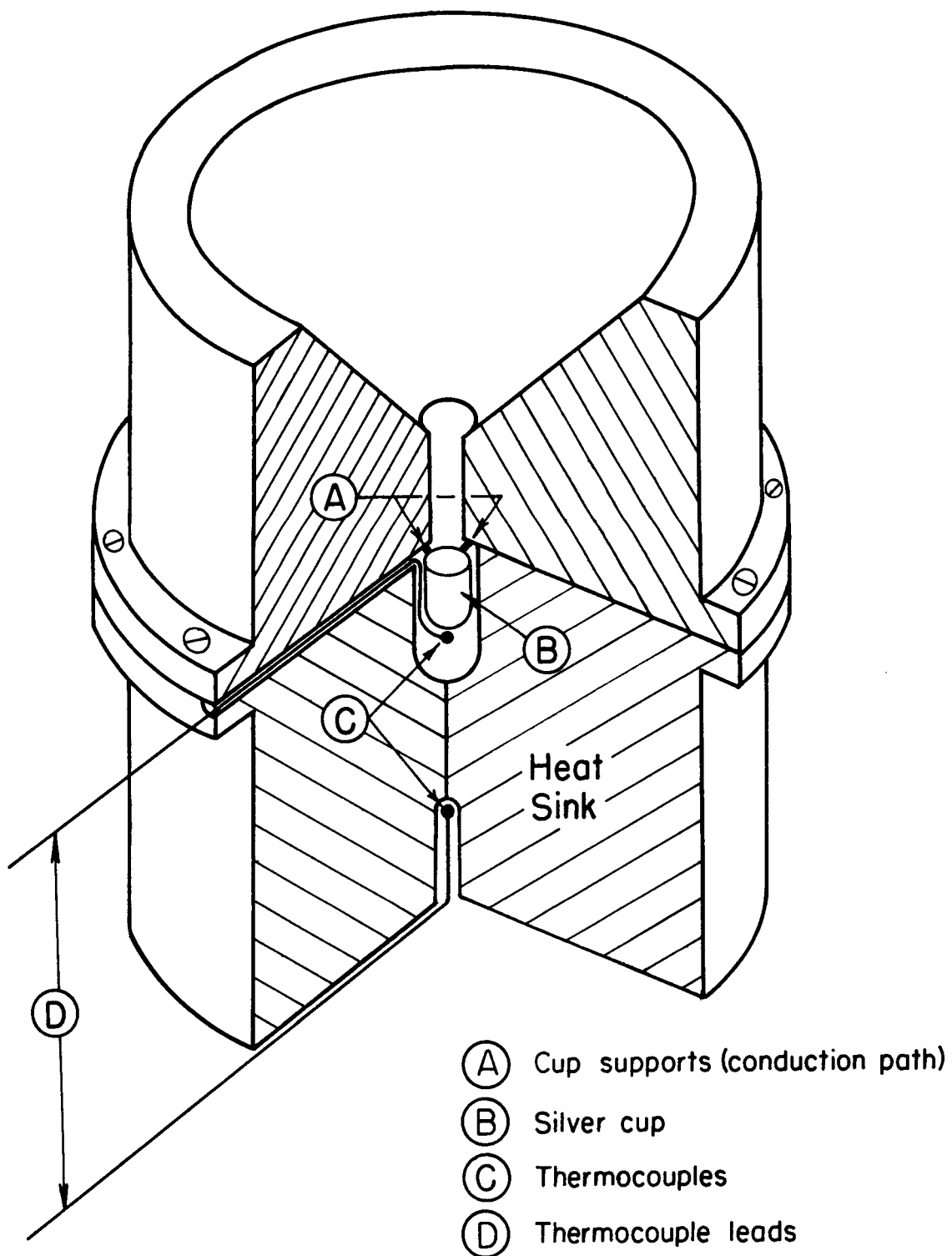


Figure 7.- Quarter-sectional drawing of the calorimeter.

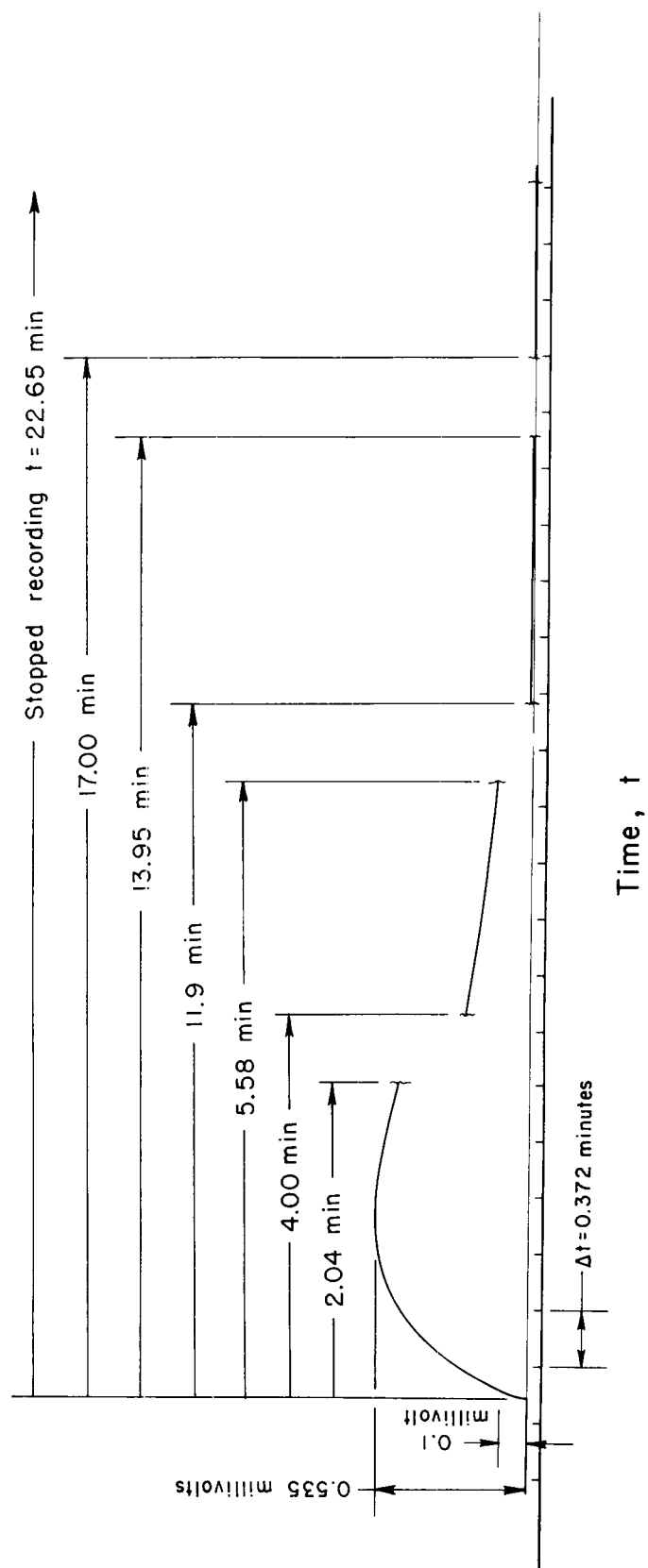


Figure 8.- Typical calorimeter heating trace.

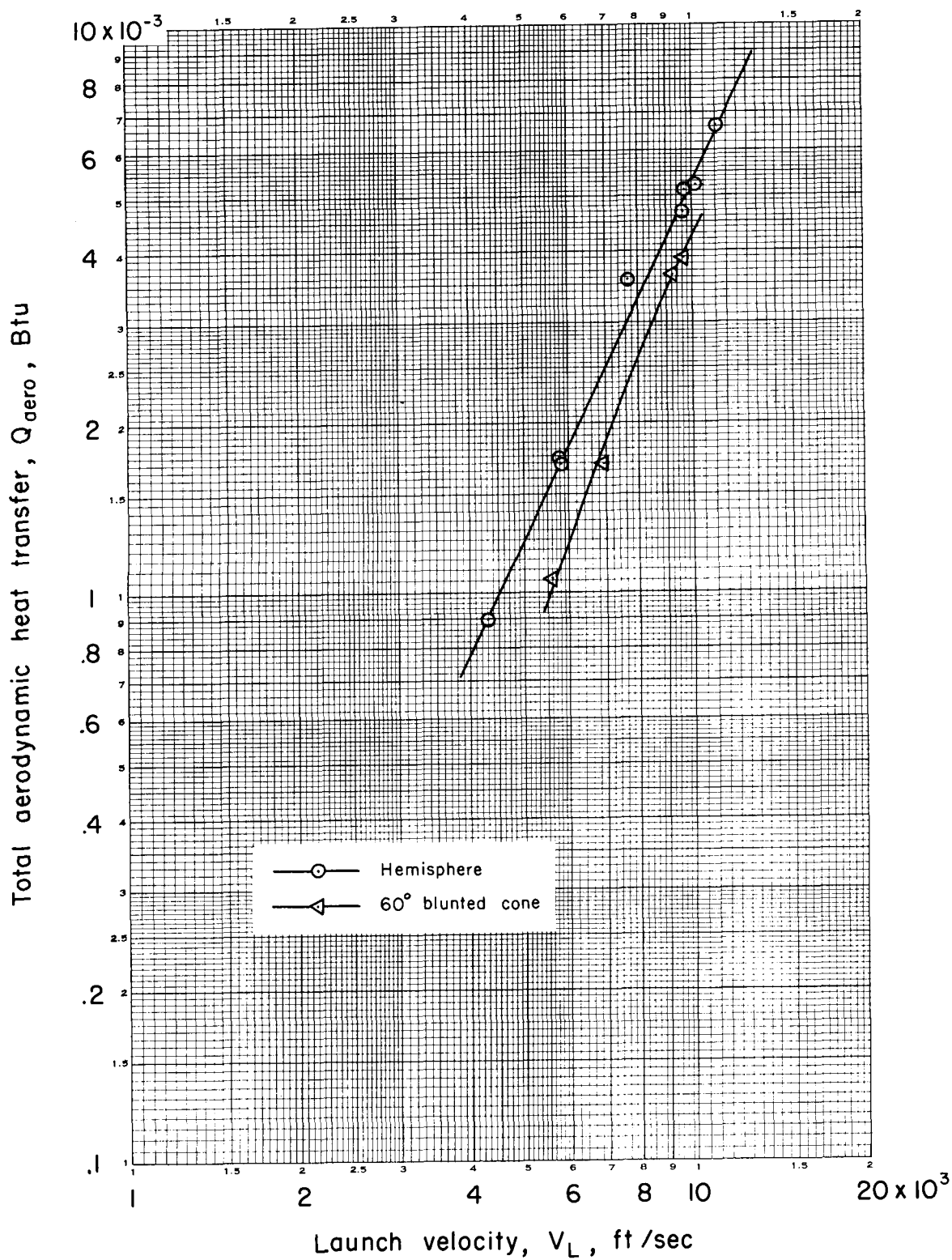


Figure 9.- Total aerodynamic heat transfer to the hemisphere and 60° blunted cone.

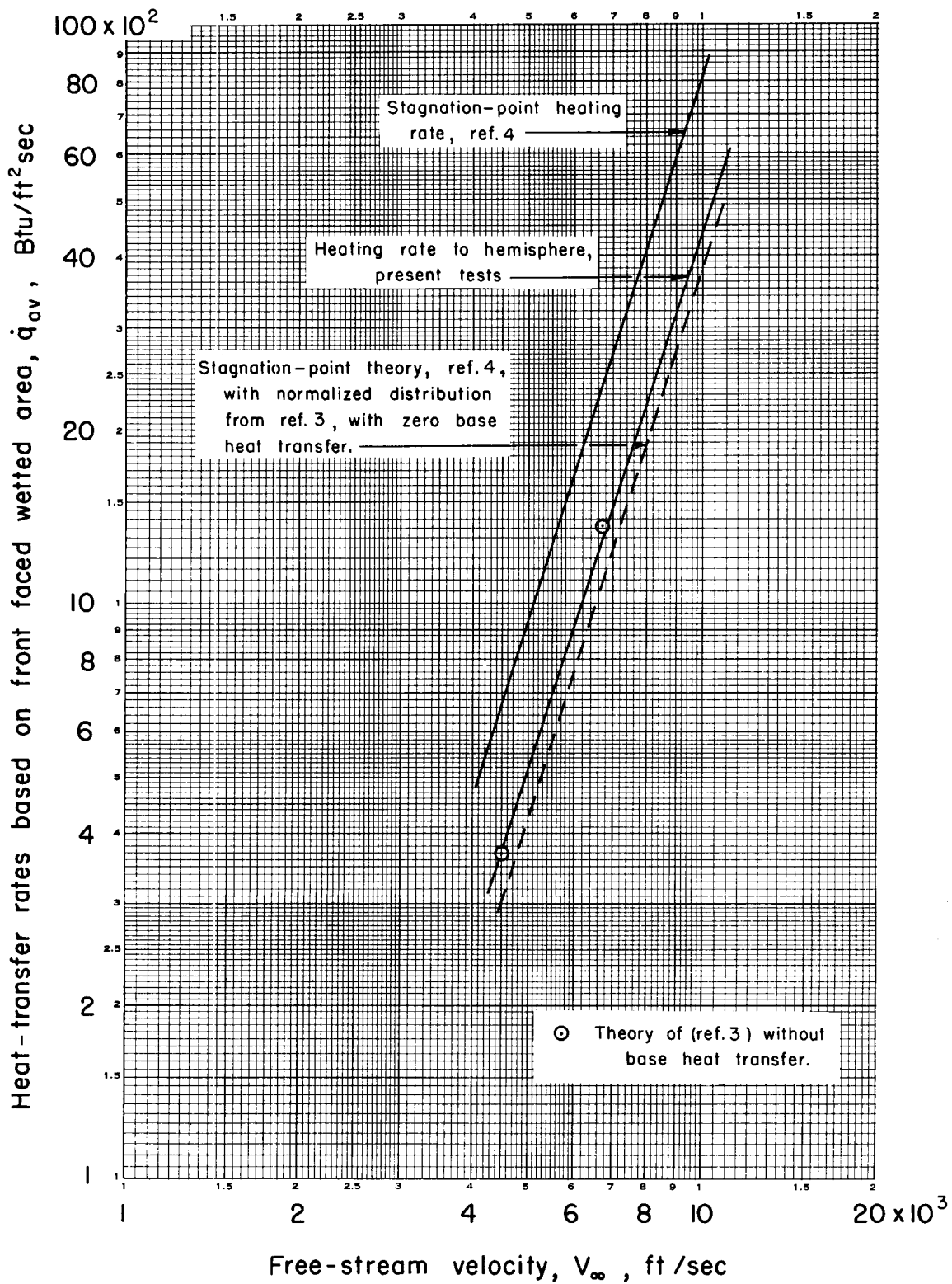
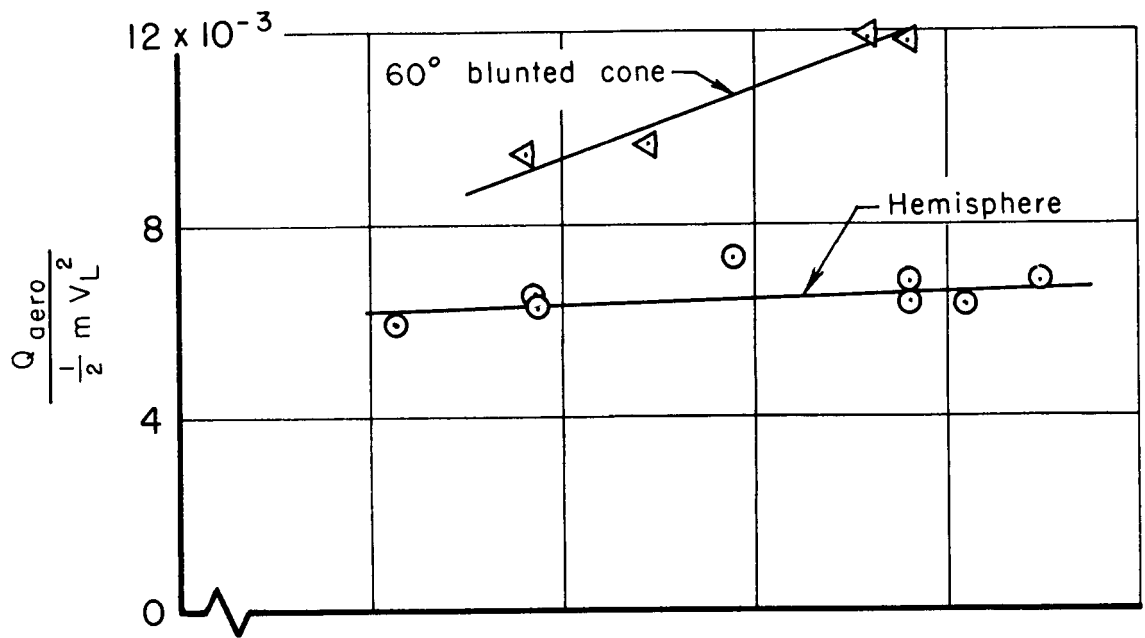
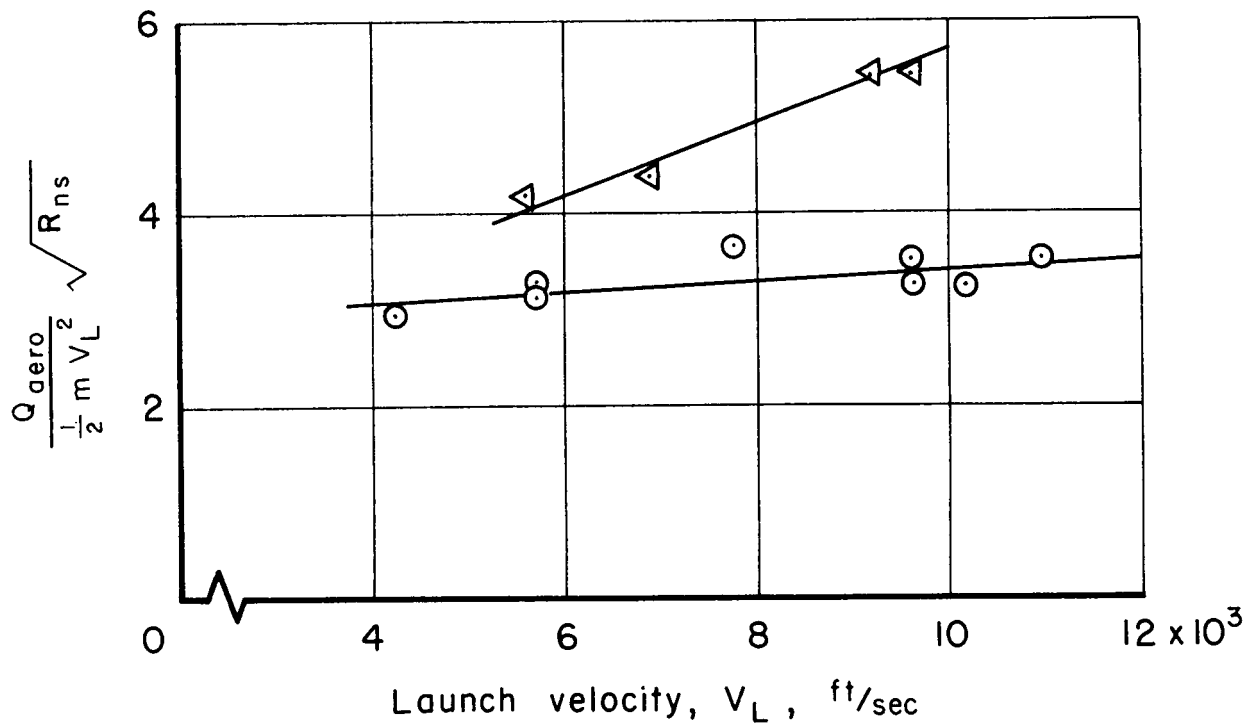


Figure 10.- Comparison of the experimental and theoretical heat transfer, based on front face wetted area, for the hemisphere configuration.



(a) Fraction of initial kinetic energy resulting in heating of the test model.



(b) Normalized fraction of initial kinetic energy resulting in heating of the test model.

Figure 11.- Comparison of total heat transfer.

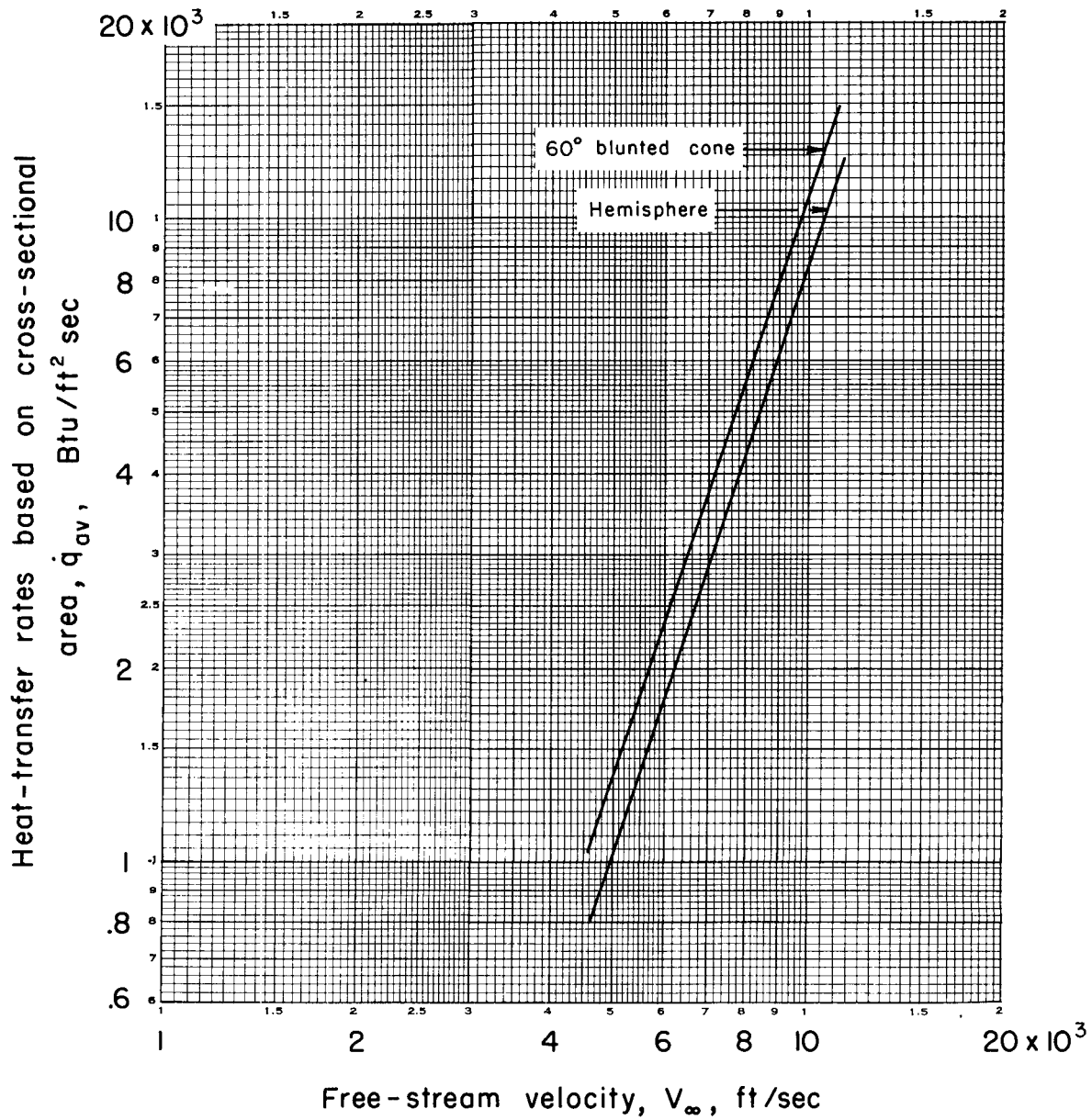


Figure 12.- Comparison of heat-transfer rates, based on the cross-sectional area, of the various configurations.

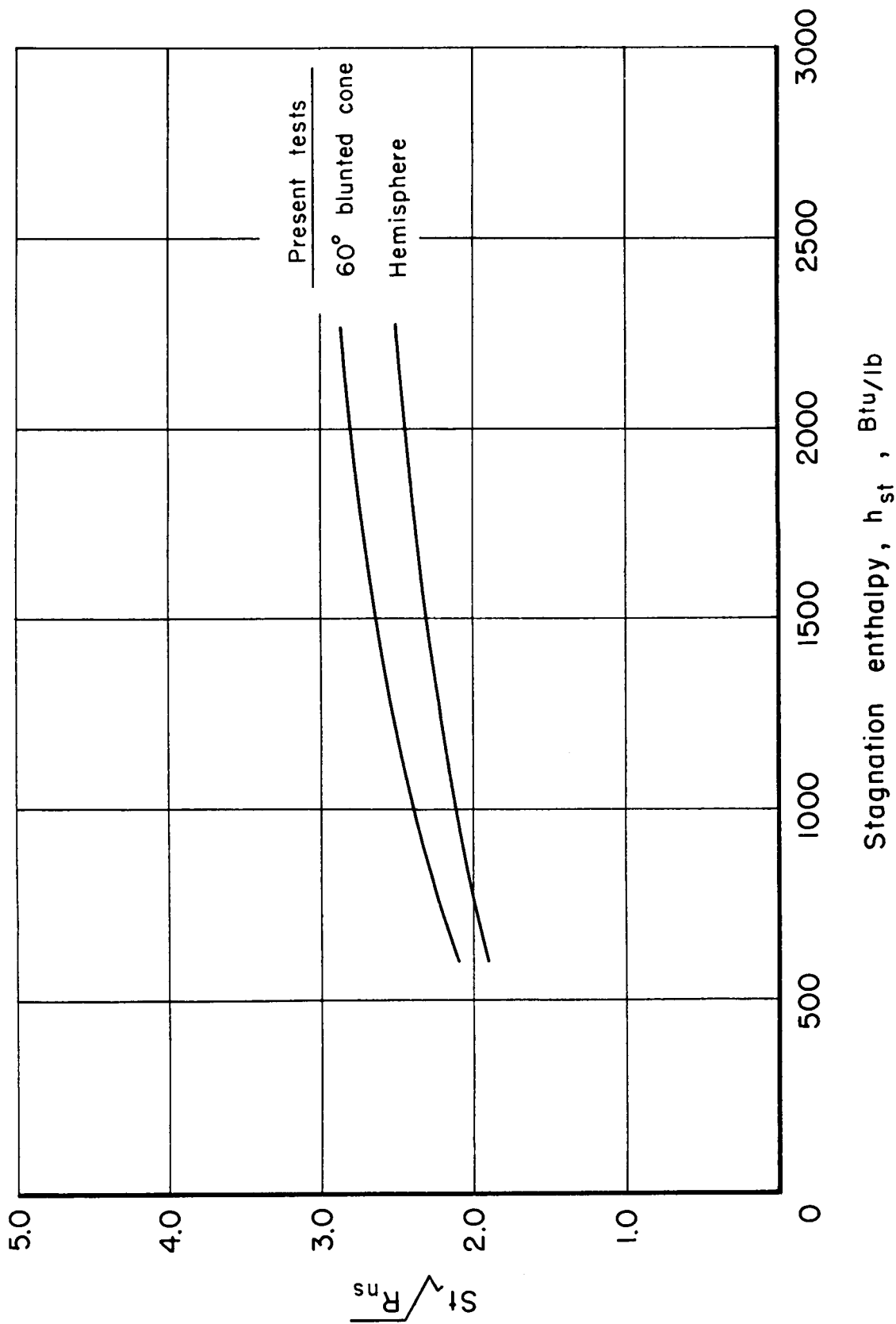


Figure 13.- The effect of stagnation enthalpy on heat-transfer parameter.

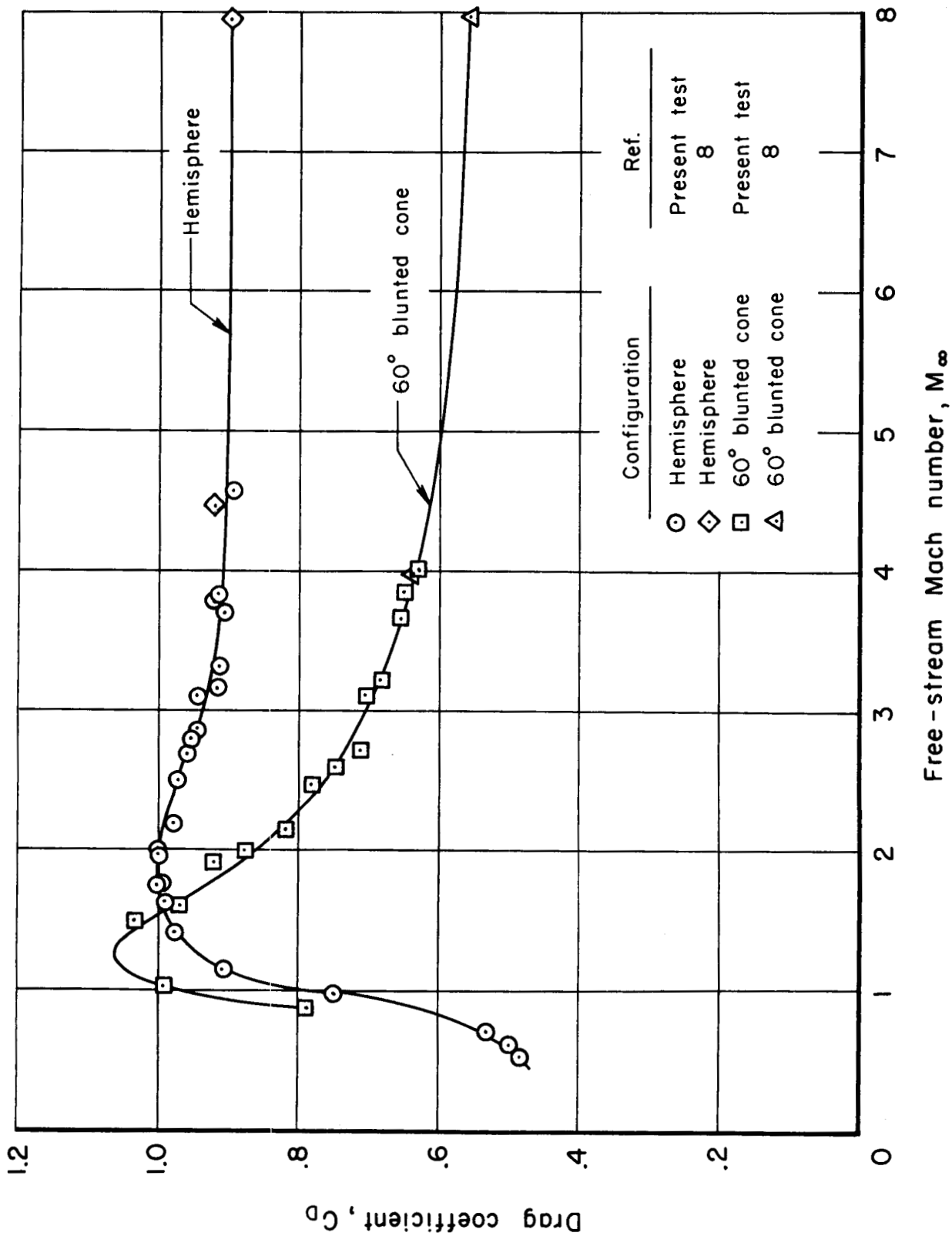


Figure 14.- Drag results of the hemisphere and 60° blunted cone.